# Influence of Manufacturing Process and Alloying Element Content on the Tribomechanical Properties of Cobalt-Based Alloys

**H. Yu**

**R. Ahmed**[1]
e-mail: r.ahmed@hw.ac.uk

School of Engineering and Physical Sciences,
Heriot-Watt University,
Edinburgh, EH14 4AS, UK

**H. de Villiers Lovelock**
Deloro Stellite,
Cheney Manor Industrial Estate,
Swindon, SN2 2PW, UK

**S. Davies**
Bodycote HIP Ltd.,
Sheffield Road,
Sheepbridge,
Chesterfield, S41 9ED, UK

*Manufacturing process routes of materials can be adapted to manipulate their microstructure and hence their tribological performance. As industrial demands push the applications of tribological materials to harsher environments of higher stress, starved lubrication, and improved life performance, manufacturing processes can be tailored to optimize their use in particular engineering applications. The aim of this paper was therefore to comprehend the structure-property relationships of a wear resistant cobalt-based alloy (Stellite 6) produced from two different processing routes of powder consolidated hot isostatic pressing (HIPing) and casting. This alloy had a nominal wt % composition of Co–28Cr–4.5W–1C, which is commonly used in wear related applications in harsh tribological environments. However, the coarse carbide structure of the cast alloy results in higher brittleness and lower toughness. Hence this research was conducted to comprehend if carbide refinement, caused by changing the processing route to HIPing, could improve the tribomechanical performance of this alloy. Microstructural and tribomechanical evaluations, which involved hardness, impact toughness, abrasive wear, sliding wear, and contact fatigue performance tests, indicated that despite the similar abrasive and sliding wear resistance of both alloys, the HIPed alloy exhibited an improved contact fatigue and impact toughness performance in comparison to the cast counterpart. This difference in behavior is discussed in terms of the structure-property relationships. Results of this research indicated that the HIPing process could provide additional impact and fatigue resistance to this alloy without compromising the hardness and the abrasive/sliding wear resistance, which makes the HIPed alloy suitable for relatively higher stress applications. Results are also compared with a previously reported investigation of the Stellite 20 alloy, which had a much higher carbide content in comparison to the Stellite 6 alloy, caused by the variation in the content of alloying elements. These results indicated that the fatigue resistance did not follow the expected trend of the improvement in impact toughness. In terms of the design process, the combination of hardness, toughness, and carbide content show a complex interdependency, where a 40% reduction in the average hardness and 60% reduction in carbide content had a more dominating effect on the contact fatigue resistance when compared with an order of magnitude improvement in the impact toughness of the HIPed Stellite 6 alloy.*
[DOI: 10.1115/1.2991122]

*Keywords: Stellite 6, HIPing, contact fatigue, abrasive wear, sliding wear*

## 1 Introduction

Stellite 6, which has a nominal wt % composition of Co–28Cr–4.5W–1C, is one of the most widely used cobalt-based alloys for industrial applications. This cobalt-based alloy[2] is generally used in power generation, marine, automotive, aerospace, and oil and gas industries to provide wear resistant components particularly in lubrication-starved, high temperature, or corrosive environments. Despite the wide ranging use of this alloy, there are limited investigations in published literature that compare the tribomechanical behavior of this particular alloy produced by two different manufacturing processes of hot isostatic pressing (HIPing) and casting. These changes in manufacturing processes dictate the structure-property relationships, and hence their tribological behavior. While industrial demands push the use of these alloys to higher stress applications, changes in manufacturing processes can be adapted to produce alloys that can deliver the required tribological performance.

Benefiting from the fcc to hcp phase transformation of cobalt, the solid solution strengthening by tungsten, and the formation of hard Cr/W-rich carbides; this alloy has a high strength and an excellent resistance to abrasive/sliding wear, galling, and high-angle erosion. This alloy is generally used in impact and fatigue resistance applications such as valve seat and gate, pump shaft and bearing, erosion shield, and rolling couples [1]. The structure-property relationships of the cast CoCr28W alloy has been a topic of research for a number of investigations [1–5]. The cast alloy exhibits a hypoeutectic microstructure with the primary fcc Co-rich dendrites surrounded by Cr-rich $M_7C_3$ ($M$=metal) eutectic carbides. With the addition of molybdenum, silicon or yttrium, $M_{23}C_6$ carbides could also be formed [6–8]. The influence of the content and morphology of the carbide on the abrasive wear of cobalt-based alloys were also a topic of research in published literature [9–15]. Various wear mechanisms during sliding wear tests, e.g., carbide fracture, carbide pullout, and ploughing on the

[1]Corresponding author.
[2]Stellite is a registered trade name of Deloro Stellite Company Inc.

Contributed by the Tribology Division of ASME for publication in the JOURNAL OF TRIBOLOGY. Manuscript received February 24, 2008; final manuscript received August 7, 2008; published online December 4, 2008. Assoc. Editor: Mitjan Kalin.

  

Table 1 The chemical compositions of cast and HIPed Stellite 6 and Stellite 20 alloys (wt %)

| | Co | Cr | W | C | Mo | Fe | Ni | Mn | Si |
|---|---|---|---|---|---|---|---|---|---|
| Cast Stellite 6 alloy | Bal. | 27.10 | 4.95 | 0.95 | 0.30 | 1.10 | 0.60 | 0.90 | 1.24 |
| HIPed Stellite 6 alloy | Bal. | 29.50 | 4.60 | 1.09 | 0.22 | 2.09 | 2.45 | 0.27 | 1.32 |
| Cast Stellite 20 [20] | Bal. | 34.50 | 16.50 | 2.39 | 0.50 | 1.50 | 1.00 | 0.60 | 0.78 |
| HIPed Stellite 20 [20] | Bal. | 31.85 | 16.30 | 2.35 | 0.27 | 2.50 | 2.28 | 0.26 | 1.00 |

matrix were previously reported [16–19]. However, investigations relating to the tribomechanical comparison of cast and HIPed Stellite 6 alloys are very limited in published literature [20,21].

A recent investigation by the authors on the influence of manufacturing processes on the tribomechanical and structure-property relationships of Stellite 20 alloys indicated that the underlying tribological failures were governed by the changes in carbide content and morphology [20]. However, Stellite 20 (wt % composition of Co–33Cr–17.5W–2.5C) has a much higher carbon and tungsten content in comparison to the Stellite 6 alloy, which significantly promotes carbide formation in the Stellite 20 alloy, and results in a hypereutectic microstructure. Due to the relatively lower carbon and tungsten content in the Stellite 6 alloy, the carbide formation is hindered in the hypoeutectic microstructure, resulting in a relatively lower hardness and an improved toughness. However, investigations relating to the influence of these relative changes in the microstructure of Stellite 6, and also those relating to the changes by varying the manufacturing process from casting to HIPing, on the tribomechanical performance are limited in published literature. Both of these aspects are considered in the current investigation. This paper provides microstructural and tribomechanical comparisons of HIPed and cast Stellite 6 alloys via scanning electron microscopy (SEM), energy dispersive X-ray spectroscopy (EDS), X-ray diffractometry (XRD), hardness, impact toughness, contact fatigue, abrasive wear, and sliding wear evaluations.

## 2 Experimental Test Procedures

**2.1 Materials and Microstructure.** Table 1 summarizes the chemical compositions of both HIPed and cast Stellite 6 alloys. The HIPed alloy was produced by canning the gas-atomized powders at a temperature and pressure of 1200°C and 100 MPa, respectively, for 4 h in a HIPing vessel. The sieve analysis of these powders (+250 $\mu$m (0.1 wt %), −250+180 $\mu$m (9.3 wt %), −180+125 $\mu$m (23.8 wt %), −125+45 $\mu$m (50.3 wt %), and −45 $\mu$m (16.4 wt %)) indicated that 75 wt % of the powder particles were in the size range of 45–180 $\mu$m. The cast alloy samples were produced via sand casting. Table 1 also shows the chemical composition of previously reported Stellite 20 alloys to aid the discussion, where the fractions of both tungsten and carbon were much higher. The microstructure of the powders and both alloys was observed via SEM using a back-scattered electron imaging (BEI) detector. The chemical compositions of different phases developed in the powders and alloys were determined via EDS and XRD with Cu-$K_\alpha$ radiation (wavelength=1.5406 Å). Image analysis was also conducted to ascertain the area fractions of individual phases.

**2.2 Hardness and Impact Tests.** The Vickers macro- and microhardness of both alloys were measured using a conventional Avery hardness tester under a load of 294 N and a Mitutoyo (MVK-H1) microhardness tester under a load of 2.94 N, respectively. Five macrohardness and ten microhardness measurements were conducted on each alloy. In order to investigate the microhardness of the individual phases in the microstructure, ten microhardness measurements under a low load (0.098 N) were also conducted on different microstructural phases of the cast alloy. The un-notched Charpy impact tests were conducted on alloy samples with dimensions of $10\times10\times55$ mm$^3$, using an Avery Charpy impact tester at an impact rate of 5 m/s. Three tests were conducted on each alloy.

**2.3 Abrasive Wear Tests.** Dry sand rubber wheel (DSRW) abrasion tests (ASTM G65 standard (Procedure B)) [22] were conducted to evaluate the abrasive wear performance of both alloys. During each test, the alloy sample with dimensions of $6\times25\times75$ mm$^3$, was forced under a load of 130 N against the rubber wheel, which rotated at a speed of $200\pm5$ rpm. The outer polyurethane rim of the wheel had a diameter of 228.6 mm and a hardness of Shore A-60. Two types of silica sand particles were used as abrasives in this investigation. Both were dry and rounded, but they were different in size distribution. 85 wt % particles of Sand A had sizes in the range of 90–180 $\mu$m. Sand B had a larger average particle size, with at least 85 wt % of particles having sizes between 150 $\mu$m and 300 $\mu$m. The silica sand was introduced between the alloy sample and the rubber wheel, with a sand flow rate of about 330 g/min. Each test lasted a total of 2000 revolutions, which was controlled by a revolution counter. Three tests were conducted on each material with Sand A and Sand B, respectively. The wear mass loss of the sample was weighed to the nearest 0.001 g. The abrasive wear test results were reported as volume loss, which were computed from the mass loss and density of the alloy.

**2.4 Sliding Wear Tests.** The sliding wear resistance of both alloys was examined via two different test methods, i.e., self-mated pin-on-disk tests and ball-on-flat tests wearing against a WC-Co ball. Both tests were conducted at room temperature on a bench mounted wear test machine. The friction force was measured via a tension-compression load cell.

The self-mated pin-on-disk tests were conducted between a pin and a disk sample under a normal load of 25 N. The alloy pin sample had a diameter of 6 mm and a length of 19 mm. The alloy disk sample had a diameter of 31 mm and a thickness of 8 mm. The average surface roughness ($R_q$) of the disk samples was 0.1 $\mu$m. This methodology was consistent with ASTM G133–02, Procedure A [23], except that the tip radius of the pin was 10 mm instead of 4.76 mm. During the test, the disk sample experienced a reciprocating sliding motion at an oscillating frequency of 5 Hz and a stroke length of 10 mm. The total sliding distance was 100 m for each test. Three tests were conducted on each alloy. The wear surfaces of the pin and the disk were measured via an interferometer (Zygo New View). The volume loss of the pin was computed from the scar diameter, and the volume loss of the disk was computed from the length of stroke and the average cross-sectional area of the wear grooves.

The ball-on-flat tests were conducted using a WC-Co ball (93.5–94.5 wt % WC and 5.5–6.5 wt % Co) and an alloy disk sample under a normal load of 25 N. The ball radius was 6.35 mm. The disk sample had the same dimensions as those used in the pin-on-disk tests. During the test, the disk sample experienced a reciprocating sliding motion at an oscillating frequency of 1 Hz, with a stroke length of 10 mm. The total sliding distance was 500 m for each test. Three tests were conducted on each alloy. The wear volume loss of the disk sample was computed from the length of the stroke and the average cross-sectional area of the wear grooves, which was measured via the interferometer.

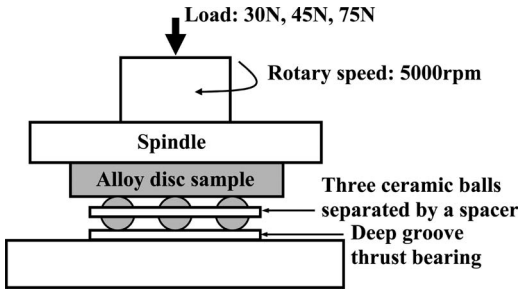


**Fig. 1 Schematic illustration of the cup assembly for the rolling contact fatigue tests**

**2.5 Rolling Contact Fatigue Tests.** The rolling contact fatigue (RCF) tests were conducted on a modified four-ball machine, as illustrated in Fig. 1, details of which can be appreciated from Stewart et al. [24]. In this configuration, three $Si_3N_4$ ceramic balls with a diameter of 4.76 mm were equispaced at 120 deg using a polymer spacer and driven by a 31 mm diameter alloy disk sample. The rotary speed of the drive shaft was set at 5000 rpm during the test, and the contact load was varied to 30 N, 45 N, and 75 N. Exxon Turbo 2389 was used as the test lubricant. The λ value, which indicates the ratio of the minimum fluid film thickness to the average surface roughness, was approximated between 1.8 and 1.9, indicating that the tests were carried out under a mixed elastohydrodynamic lubrication (EHL) regime, i.e., partial asperity contact during the tests. The RCF failure was detected by the increase in the vibration amplitude of the cup assembly above a preset level.

## 3 Results

**3.1 Microstructure and Phase Analysis.** Figures 2 and 3 provide the SEM and XRD comparison of the cast and HIPed alloys. Figure 2(*a*) shows the SEM of the dendritic microstructure on the spherical surface of the gas-atomized powder. Figure 2(*b*) and 2(*c*) show the hypoeutectic microstructure of the cast alloy, which consists of Cr-rich carbides (dark phase), W-rich carbides (bright phase), and the Co-rich dendritic matrix (gray region). Figure 2(*d*) shows the SEM observation of the HIPed alloy, with finer carbides (dark phase) uniformly distributed in a Co-rich matrix (gray region). The image analysis results of the area fractions of various phases are presented in Table 2. Previously reported [20] image analysis results for Stellite 20 alloys are also presented in this table to aid the discussion.

**3.2 Hardness and Impact Toughness.** Table 3 summarizes the average hardness and Charpy impact energy results of Stellite 6 alloys. The HIPed alloy had a slightly higher hardness than the cast alloy. The Cr-rich carbides in the cast alloy (dark phase in Fig. 2(*c*)) had a much higher average microhardness than the Co-rich matrix (gray region in Fig. 2(*c*)). The Charpy impact energy of the HIPed alloy was almost an order of magnitude higher than the cast alloy. The fractographs of failed areas after the Charpy

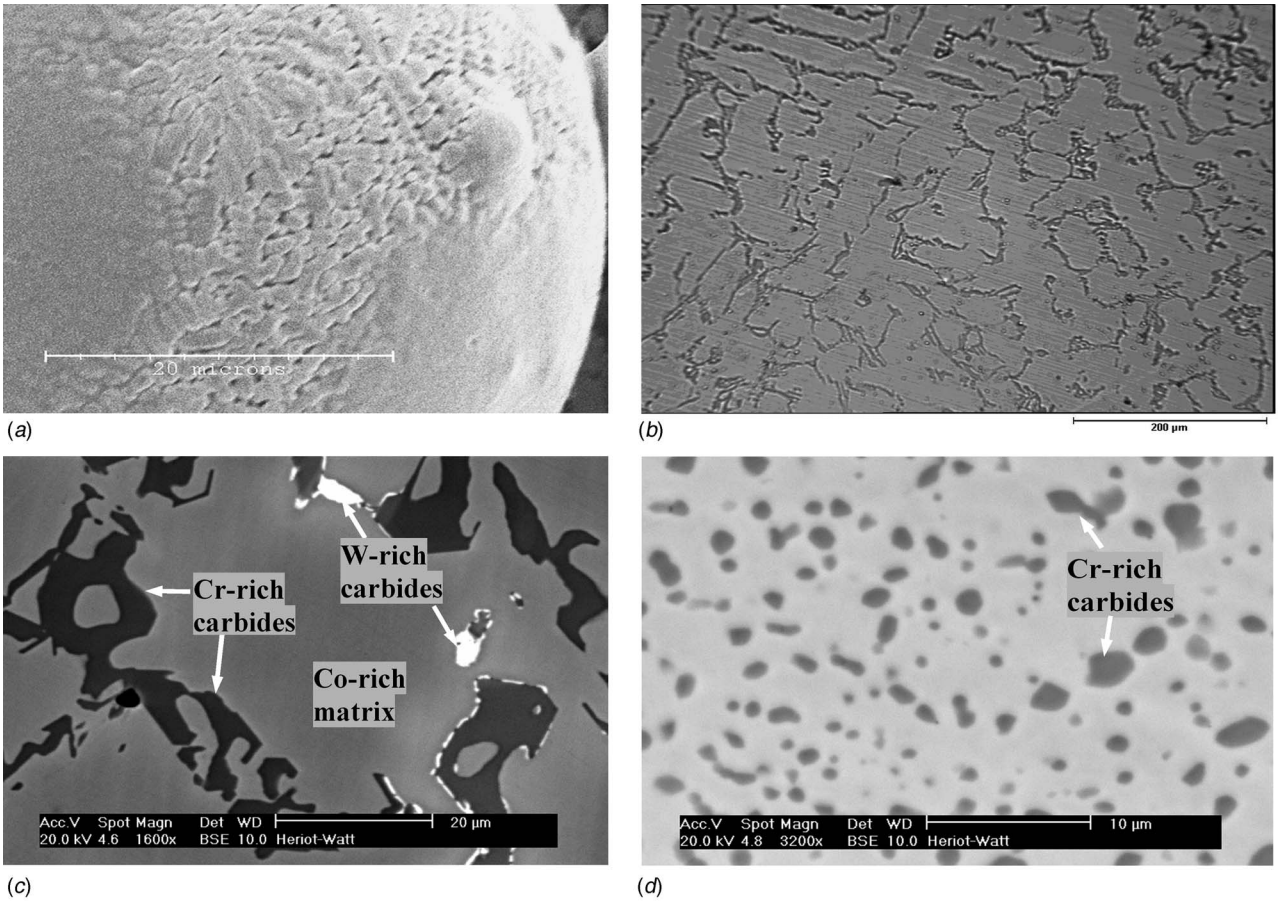


**Fig. 2 The images showing (*a*) the morphology of the alloy powder, the microstructure of (*b*) and (*c*) cast Stellite 6 alloy, and (*d*) HIPed Stellite 6 alloy**

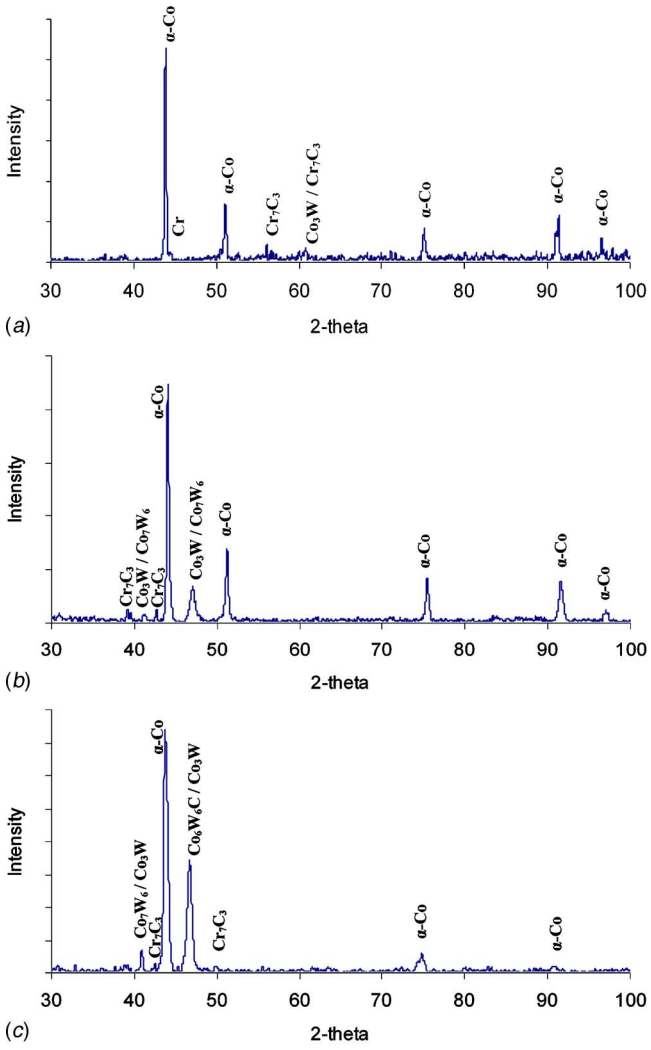


**Fig. 3 The XRD pattern of the (*a*) alloy powder, (*b*) HIPed Stellite 6 alloy, and (*c*) cast Stellite 6 alloy**

tests are presented in Fig. 4. Previously reported [20] average values of the hardness and toughness of Stellite 20 alloys are also presented in Table 3 for comparison.

**3.3 Abrasive Wear Performance.** The average abrasive wear volume loss of both alloys after the DSRW tests is shown in Fig. 5. Both alloys had a slightly higher wear loss when finer sand (Sand A) was used. The HIPed alloy had a slightly lower wear loss than the cast alloy for both types of sand used in this investigation. Figure 6 presents the typical wear scars of both alloys after the tests.

**3.4 Pin-On-Disk Wear Performance.** The volume loss results of both alloys after the pin-on-disk tests are shown in Fig. 7. The wear loss of the cast pin was lower than that of the HIPed pin. The cast disk, however, suffered more wear loss, which resulted in a similar total wear loss of both alloys. Figures 8(*a*)–8(*d*) shows typical wear scars on the surface of pins and disks. The average friction coefficient during the tests on cast and HIPed alloys was 0.42 and 0.47, respectively. The observations of the wear scars indicated that both the cast and the HIPed pins were worn flat after the test, while the cast disk had a deeper wear groove than the HIPed disk. Wear debris produced after the tests was a mixture of a platelike delamination and finer (crushed) debris.

**3.5 Ball-On-Flat Wear Performance.** The wear volume loss results after ball-on-flat tests are also presented in Fig. 7. The average volume loss of the HIPed alloy was more than that of the cast alloy. The SEM observations of the wear surfaces of both alloys are shown in Figs. 8(*e*) and 8(*f*). The wear grooves of the HIPed alloy were wider and deeper than those of the cast alloy. Although it was difficult to take a precise measurement of the ball material loss, the observations on the ball surface indicated that there was some material removal on the surface of the WC-Co ball wearing against the cast disk, while the WC-Co ball wearing against the HIPed disk was almost unworn. Therefore the total volume loss of the test couples could be similar for both alloys. The average friction coefficient during the tests was approximately 0.59 for both alloys. Platelike debris fragments with a relatively large aspect ratio were observed after the test.

**3.6 Rolling Contact Fatigue Performance.** The RCF test results are shown in Fig. 9. This figure also summarizes the previously reported RCF performance results of cast and HIPed Stellite 20 alloys to aid the discussion [20]. The stress cycles to fatigue failure for the HIPed alloy were higher than those of the cast alloy under a range of stress levels considered in this investigation. Figure 10 presents the observations of the failed areas. Cast alloy failed by delamination at an approximate depth of 32–70 $\mu$m, whereas the HIPed alloy failed by spalling at an approximate depth of 35–45 $\mu$m. Table 4 summarizes the contact parameters

**Table 2 The volume fraction of individual phases in cast and HIPed Stellite alloys**

| | Cr-rich carbides (Dark phase) | W-rich carbides (Bright phase) | Co-rich matrix (Grey region) |
|---|---|---|---|
| Cast Stellite 6 alloy | 14.5 ± 6.6% | 1.0 ± 0.5% | 84.5 ± 7.0% |
| HIPed Stellite 6 alloy | 17.9 ± 1.7% | 0.0% | 82.1 ± 1.7% |
| Cast Stellite 20 alloy [20] | 24.5 ± 2% | 18.1 ± 0.2% | 57.4 ± 1.8% |
| HIPed Stellite 20 alloy [20] | 24.2 ± 1% | 24.7 ± .0.7% | 51.1 ± 1.4% |

**Table 3 The hardness and un-notched Charpy impact energy of cast and HIPed Stellite alloys**

| | Microhardness (HV, 0.098 N) | Macrohardness (HV, 294 N) | Microhardness (HV, 2.94 N) | Un-notched Charpy impact energy (J) |
|---|---|---|---|---|
| HIPed Stellite 6 alloy | | 414.20 ± 7.90 | 419.10 ± 9.90 | 109.14 ± 35.83 |
| Cast Stellite 6 alloy: | | 408.00 ± 3.81 | 402.60 ± 20.97 | 12.20 ± 2.41 |
| Cr-rich carbide | 1198.8 ± 289.2 | | | |
| Co-rich matrix | 325.5 ± 39.3 | | | |
| HIPed Stellite 20 alloy [20] | | 675 ± 17 | 704 ± 15 | 9.26 ± 2.18 |
| Cast Stellite 20 alloy [20] | | 653 ± 18 | 759 ± 98 | 1.36 ± 0 |

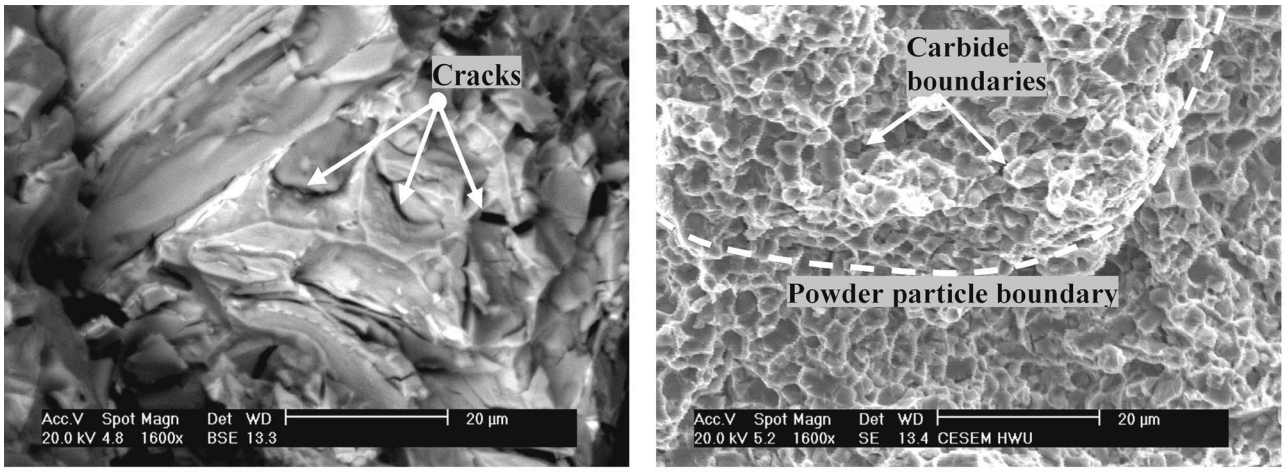


(*a*) (*b*)

**Fig. 4 The fractographs after the un-notched Charpy impact tests on (*a*) the cast Stellite 6 alloy and (*b*) the HIPed Stellite 6 alloy**

during the tests. The depths of the orthogonal shear stress, $Z_{\text{orth(max)}}$, and maximum shear stress, $Z_{\tau(\max)}$, are given by the following equations [25]:

$$Z_{\text{orth(max)}} \cong 0.35a \tag{1}$$

$$Z_{\tau(\max)} \cong 0.48a \tag{2}$$

where $a$ is the radius of the contact area, which is given by the Hertzian point contact equation [26]

$$a = \left(\frac{3wr}{4E^*}\right)^{1/3} \tag{3}$$

where $w$ is the normal load, $r$ is the radius of the ceramic ball, and $E^*$ is the combined Young's modulus, which depends on Young's modulus and Poisson's ratio of the ceramic ball and CoCr28W alloy. The maximum contact stress, $P_0$, is given by the following equation:

$$P_0 = \frac{3w}{2\pi a^2} \tag{4}$$

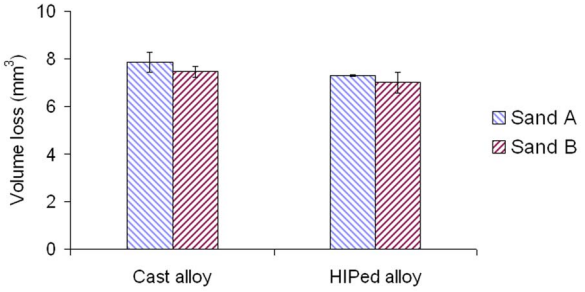


**Fig. 5 The average volume loss of cast and HIPed Stellite 6 alloys after dry sand rubber wheel tests**

## 4 Discussion

**4.1 Microstructure.** The cast CoCr28W alloy had a hypoeutectic microstructure (Figs. 2(*b*) and 2(*c*)), which consists of Co-rich dendrites (gray region), set in lamellar eutectic Cr-rich (dark phase) and W-rich (bright phase) carbides. The Cr-rich eutectic carbide had a composition of $(Cr_{0.71}Co_{0.25}W_{0.03}Fe_{0.005})_7C_3$, as approximated by the EDS analysis. The XRD analysis (Fig. 3(*c*)) revealed that the carbides were $Cr_7C_3$ and $Co_6W_6C$, while $\alpha$-Co (fcc) was the primary phase in the solid solution, together with the intermetallic compounds, $Co_3W$ and $Co_7W_6$. This dendritic microstructure is typical of the cast CoCr28W alloy in which the

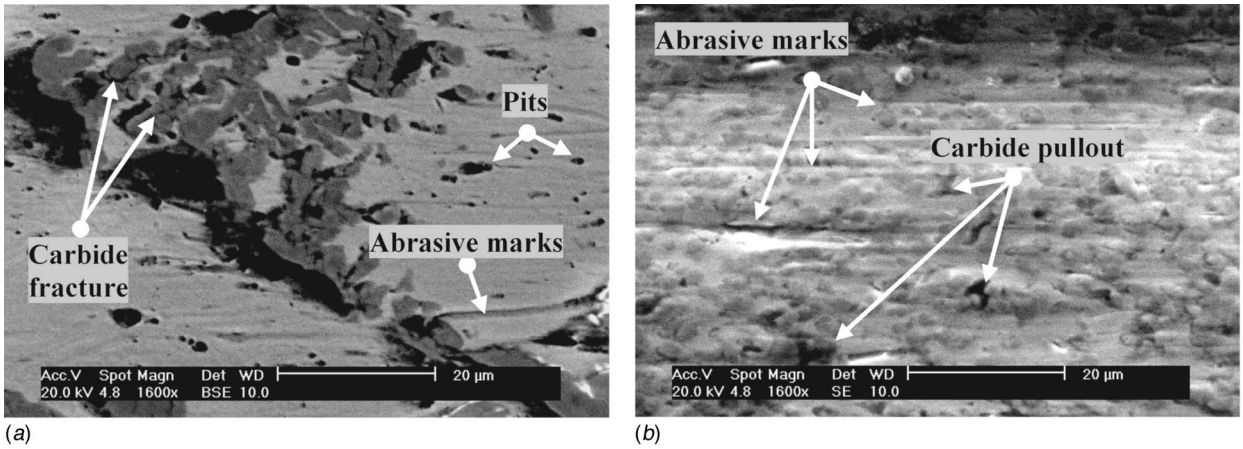


(*a*) (*b*)

**Fig. 6 The wear scar after dry sand rubber wheel tests of the (*a*) cast Stellite 6 alloy and the (*b*) HIPed Stellite 6 alloy**

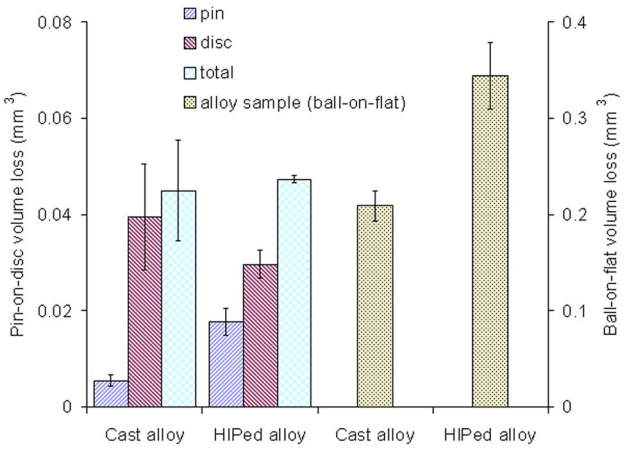


**Fig. 7 The wear loss of the cast and HIPed Stellite 6 alloys after the pin-on-disk and ball-on-flat tests**

carbide and grain size can be controlled by the rate of cooling. Within the family of cast cobalt-based alloys, the relatively large carbide size seen in the cast microstructure indicated slow freezing during the casting process. The microstructure of cast Stellite 6 alloys was a topic of research for a number of investigations and further details of the influence of the cooling rate on the grain size of cast cobalt-based alloys can be appreciated elsewhere [13]. The scope of the discussion here is therefore its microstructural comparison with the HIPed counterpart in terms of understanding the structure-property relationships during tribomechanical performance.

The HIPed alloy had a much finer microstructure (Fig. 2(*d*)) with Cr-rich carbides (dark phase) uniformly distributed in the matrix. The typical carbide size was 1–3 $\mu$m, which was much finer than the cast counterpart. There was no bright (W-rich) phase observed in the HIPed microstructure, which could be attributed to the fast solidification in the powder manufacturing process, restricting the segregation of W-rich zones. Subsequently during HIPing of the powder, tungsten remained evenly distributed throughout the alloy because its large atomic radius hinders diffusion. This evolution of the HIPed microstructure was therefore fundamentally different from the dendritic microstructure of the cast alloy, which was caused by the rejection of elemental species in the melt during the crystal growth of Co-rich dendrites. Hence above the liquidus line of this complex Co alloy, elemental species were free to arrange themselves depending on the thermal kinetics of the mold without any dependency on diffusion, and hence a truly three-dimensional network of carbides was formed.

Contrary to this, in the case of HIPed microstructure, the primary dendrites formed on the alloy powder (Fig. 2(*a*)), and the carbides in the powder particles (Fig. 3(*a*)) promoted carbide growth due to the diffusion of carbon and other elemental species within and across the individual powder particle boundaries. As this diffusion process is time, temperature, and pressure dependent during HIPing, and the HIPing temperature (1200°C in this investigation) was lower than the melting point of the powder, carbide growth was sluggish when compared with casting. Hence the size of individual carbide particles was much smaller than the cast counterpart. Although not reported in Sec. 3, authors also found that re-HIPing the HIPed alloy under similar conditions as were reported earlier in Sec. 2.1 did not substantially increase the average carbide size, indicating that carbide growth was more dependent on temperature than time during the HIPing process. The XRD analysis (Fig. 3(*b*)) revealed that the possible phases in the HIPed alloy were $Cr_7C_3$, $\alpha$-Co, $Co_3W$, and $Co_7W_6$, which were similar to those in the cast alloy, except the absence of $Co_6W_6C$. The intermetallic compound, $Co_7W_6$, was not identified in the atomized powder, indicating that it was formed during the HIPing process. The pure Cr phase in the powder, which formed due to the rapid solidification, was not identified in the HIPed alloy, indicating that it either combined with the cobalt matrix, or formed carbides.

The image analysis (Table 2) showed that the cast alloy had an approximate total carbide fraction of 15.5%, which was slightly less than that of the HIPed alloy (17.9%). These values indicated on average a 63% reduction in the carbide content when compared with the Stellite 20 alloy, which can be attributed to the lower carbon and tungsten content in the Stellite 6 alloys. These differences in the microstructure, carbide content, and morphology had a significant influence on the tribomechanical performance, as discussed in the following sections.

**4.2 Hardness.** In comparison to the Stellite 20 alloy, the hardness of Stellite 6 alloy (Table 3) was relatively lower due to its lower carbide content (Table 2). It is widely accepted that the contents of carbon and tungsten play a dominant role in the hardness of cobalt-based alloys. Both the formation of hard carbides and solid solution strengthening by tungsten can enhance the hardness of cobalt-based alloys [27–29]. For the Stellite 6 alloys considered in this investigation, the $M_7C_3$ and $Co_6W_6C$ carbides, as well as the intermetallic compounds $Co_3W$ and $Co_7W_6$, were all beneficial to their hardness. As there were small differences between the chemical compositions of the cast and HIPed Stellite 6 alloys, especially the contents of tungsten and carbon, both alloys had similar hardness at micro or macro levels. The HIPed alloy, however, was marginally harder than the cast alloy, mainly due to its slightly higher fraction of carbides (Table 2). Previous investigations have indicated that the differences in microstructure might also affect the hardness of cobalt-based alloys [3,30]. In this investigation, both alloys had quite different microstructures, especially the shape, size, and distribution of the carbides. However, their hardness was similar. In comparison to the hardness results of the Stellite 20 alloy, the average hardness was reduced by 41% due to the reduction in carbon and tungsten content in the Stellite 6 alloy. Hence, it can be appreciated that instead of the manufacturing route, the contents of tungsten and carbon had a more significant influence on the average hardness of these alloys.

It was difficult to measure the individual hardness of the matrix and carbide phases in the HIPed alloy using the Vickers microhardness method even at the lower load of 0.098N, as the indentation diagonal length was typically 7 $\mu$m, which was larger than the carbide size (1–3 $\mu$m, Fig. 2(*d*)) and the spaces between them (4–7 $\mu$m). However the relatively coarser carbide size (5–20 $\mu$m) in the cast alloy made it possible to measure the microhardness of individual phases. The experimentally measured matrix and carbide hardness in the cast alloy were HV325.5 ± 39.3 and HV1198.8 ± 289.2 (Table 3), respectively. The hardness of individual phases, together with their respective fractions of 84.5% and 15.5% (Table 2), could be used to approximate an average hardness of HV461. This assessment methodology based on the area fraction of constituents in multiphase alloys is consistent with the property evaluation, as indicated by Ghar [31]. Similar techniques, based on the inverse relationship between the volume fraction and the property of the cobalt-based alloy, could also be applied to evaluate the hardness, indicating an approximate hardness of HV367. However, the experimental result (HV402.6 ± 21.0) was close to the average of these two evaluations (HV414) rather than any of them, indicating a complex relationship between the area fraction and hardness of individual phases in these alloys.

**4.3 Charpy Impact Energy.** The Charpy impact energy absorption represents the impact toughness of the material under dynamic condition. Although most cobalt-based hard alloys have a high strength, with a typical ultimate tensile strength (UTS) of 766–897 MPa [29] and 1265–1375 MPa [27] for the cast and HIPed alloys, respectively, the toughness of the cast alloy is usually much lower than the HIPed alloy due to the brittle eutectic

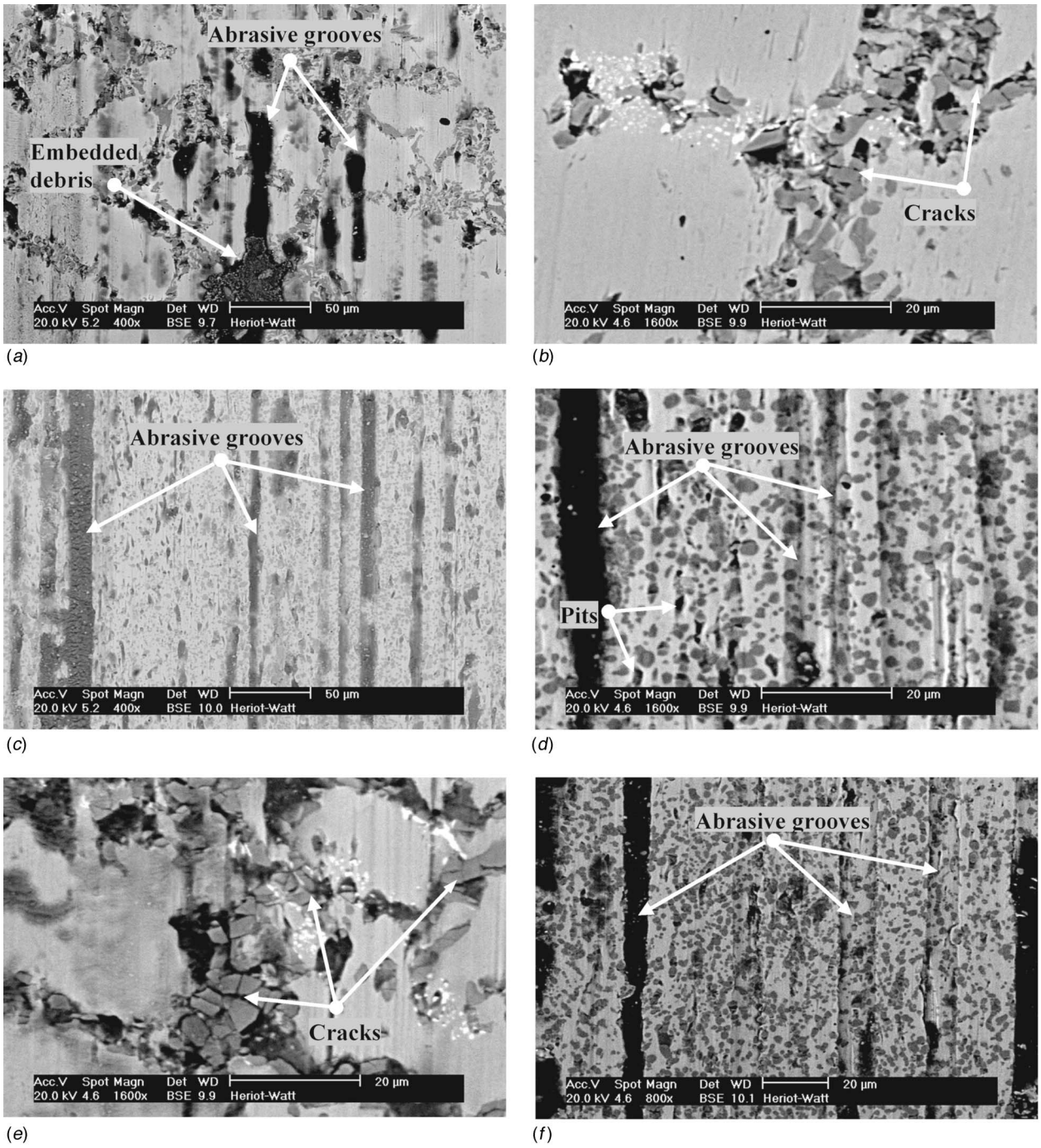


**Fig. 8 The SEM images showing the wear scars after pin-on-disk tests of the (*a*) cast alloy pin, (*b*) cast alloy disk, (*c*) HIPed alloy pin, and (*d*) HIPed alloy disk, and the wear scars after ball-on-flat tests of (*e*) cast alloy disc and (*f*) HIPed alloy disc**

microstructure of the cast alloy, which results in elongation values generally less than 1% [27,29]. The impact toughness results summarized in Table 3 indicate an order of magnitude improvement for the HIPed alloy. This improvement is consistent with the previously reported results of the HIPed 20 alloy, with the exception that the overall impact toughness of the Stellite 20 alloy (cast Stellite 20 impact toughness=1.36 J and HIPed Stellite 20 impact toughness=9.26) was significantly lower than that of the Stellite 6 alloy. Similarly, there was an order of magnitude improvement (from 9 J to 109 J) in the impact toughness of the HIPed Stellite 6 alloy, when compared with the HIPed Stellite 20 alloy. This difference in behavior between HIPed Stellite 6 and 20 alloys is attributed to the absence of W-rich carbides and the lower carbide content in the HIPed Stellite 6 alloy. In terms of the design process, an order of magnitude improvement in the impact toughness indicates substantial expected gains in the fatigue performance of the Stellite 6 alloy. However, as discussed in Sec. 4.7, it was a combination of factors, such as hardness, carbide content, and impact resistance, which dictated the fatigue performance of these alloys, which was governed not only by the manufacturing processing route but also by the content of alloying elements.

During the impact test, a brittle fracture initiated along and within the coarse carbides in the cast Stellite 6 alloy, followed by rapid crack propagation, as indicated by a number of micro- and macrocracks observed in Fig. 4(*a*). Although some bright (W-rich) carbides are also visible in Fig. 4(*a*), most cracks followed the

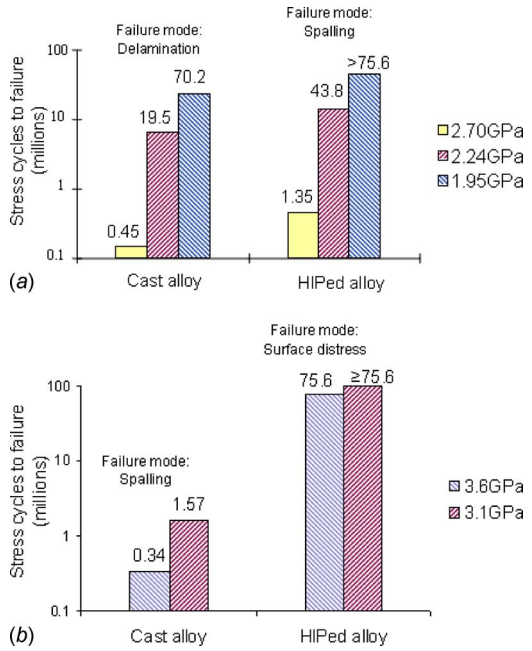


**Fig. 9 Stress cycles to failure of cast and HIPed alloys after the rolling contact fatigue tests: (*a*) Stellite 6 alloys and (*b*) Stellite 20 alloys**

eutectic network of Cr-rich carbides. The SEM observations (Fig. 4(*b*)) indicated that the fracture within the carbide particles of the HIPed alloy was not appreciable. The cracks followed the carbide/matrix boundaries and the powder particle boundaries, as indicated in Fig. 4(*b*). A typical powder particle size of approximately 80 $\mu$m can be inferred from Fig. 4(*b*), which is consistent with the sieve analysis of the powder (Sec. 2.1). Hence, the particle powder boundary was the preferred propagation route for the microcracks, which initiated at the carbide/matrix boundaries in the HIPed alloy. Although no appreciable porosity was observed in the HIPed alloy, indicating a full compaction during the HIPing process, the powder particle boundary route of cracks indicates that further optimization of HIPing conditions to provide better bonding between the powder particles could further improve the impact toughness of the HIPed alloys. The finer microstructure

**Table 4 The contact parameters during the rolling contact fatigue tests**

| Total load (N) | 30 | 45 | 75 |
|---|---|---|---|
| Contact stress $P_0$ (GPa)—Eq. (4) | 1.95 | 2.24 | 2.70 |
| Contact width $2a$($\mu$m)—Eq. (3) | 96 | 110 | 132 |
| Orthogonal shear stress depth ($\mu$m)—Eq. (1) | 17 | 19 | 23 |
| Maximum shear stress depth ($\mu$m)—Eq. (2) | 23 | 27 | 32 |

along with the matrix ductility provided the crack arrest mechanism for the HIPed alloy. As the fine carbides in the HIPed alloy were well separated by the Co-rich matrix, crack propagation in the matrix was hindered due to matrix ductility and solid solution strengthening, thereby improving the impact resistance of the HIPed alloy. Contrary to this, although the matrix in the cast alloy had similar composition, and hence was expected to provide similar assistance for the crack arrest mechanism, the preferred propagation route was within the large eutectic carbide net rather than the carbide/matrix boundary or through the matrix. Therefore once cracks initiated in the cast alloy, they readily propagated to form macrocracks following the eutectic net, with little resistance from the matrix.

In terms of the tribological design process, the fracture mechanics approach based on fracture toughness ($K_{1C}$) is more quantitative than the use of impact toughness (based on the Charpy or similar impact tests) values to characterize the wear process. Nevertheless, Charpy impact tests provide useful and unique information about the impact energy at high strain rates. Several authors have thus attempted to correlate the Charpy impact test results with the fracture toughness values for a number of engineering materials [32–39]. These investigations have indicated that such correlations are however not general, but relate to a family or families of alloys, and are best applied to the prediction of lower-bound values [32–34]. Such relations are more common in ductile materials, which show ductile to brittle transition, e.g., high and low strength steels [35,36], turbine rotors [37], and weld alloys [38,39]. Attempts were also made to correlate such relations in composite alloys (e.g.,WC-6 wt %Co) [40]. However, no such correlation exists in published literature for the cobalt-based alloys, and furthermore this investigation related to un-notched samples instead of the commonly used V-notched samples. Therefore only qualitative comparisons are possible, indicating that the

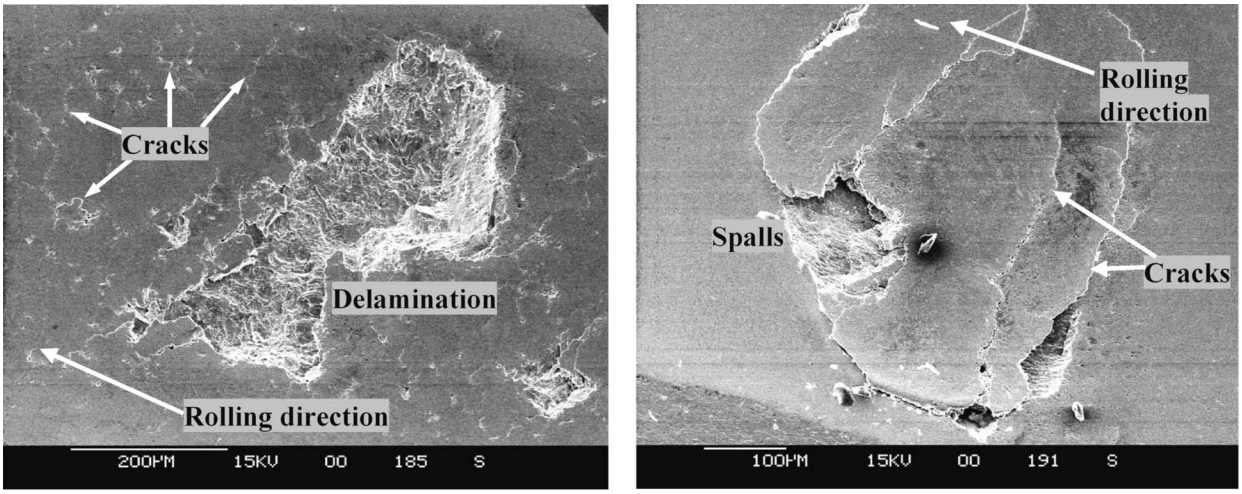


**Fig. 10 The failure areas after rolling contact fatigue tests of the (*a*) cast Stellite 6 alloy, 2.24 GPa, and (*b*) HIPed Stellite 6 alloy, 2.24 GPa**

increase in fracture toughness generally results in the increase in impact energy [34]. For qualitative purposes, an increase in the un-notched impact energy of almost an order of magnitude (Table 3) in the HIPed alloy will substantially increase its fracture toughness, which can have significant influence on the wear (abrasive, sliding, and fatigue) resistance and underpinning failure mechanisms.

**4.4 Abrasive Wear Performance.** The abrasive wear of engineering material is generally known to vary inversely with its hardness if the abrasive wear is caused by plastic deformation, whereas if abrasive wear occurs due to brittle fracture, the wear loss is usually higher and has an inverse correlation with some power of material's toughness [26]. Previous investigations have indicated that for low stress abrasive wear resistance, e.g., tests conducted via ASTM G65 (Procedure B), the wear resistance of the cast and welded cobalt-based alloys depend on the carbide size and abrasive particle properties, e.g., its type (silica sand (quartz) and alumina), size, shape, and hardness. Generally the wear resistance increases with carbide coarsening [10,15], decreasing abrasive particle size [10,14], and decreasing abrasive hardness [14]. These investigations have indicated that changes in failure mechanisms are responsible for the differences in the abrasive wear performance, e.g., micromachining dominates the abrasive wear process for relatively harder abrasive particles (alumina) [14,15], whereas carbide fracture is the dominant wear mechanism with relatively softer abrasives (silica). Furthermore, it was indicated that the cast alloy hardness can be used as a crude measure of abrasive wear resistance in a low stress abrasive wear process, whereas for the high stress abrasive wear process (e.g., via ASTM B611), both hardness and fracture toughness become critical.

Although both the cast and the HIPed Stellite 6 alloys showed similar abrasive wear resistance in this comparative investigation, their dominant wear mechanisms were different. Figure 6(*a*) shows cracks on the carbide grains, and abrasive marks and pits in the matrix region, indicating that the abrasive wear of the cast alloy involved both the brittle fracture of carbides and the microcutting of the matrix. The angularities of the abrasive sand particles could result in a high normal load on the eutectic carbide grains. If the normal load was high enough to exceed a critical value, $w^*$, cracks would form [26]. The onset of cracks depend on the fracture toughness of the alloy, $K_{IC}$, and on its hardness, $H$.

$$w^* \propto \left(\frac{K_{IC}}{H}\right)^3 K_{IC} \tag{5}$$

However brittle fracture on the coarse carbides did not account for a large amount of material removal in the cast alloy because the carbides were interlocked in the matrix even after they fractured (Fig. 6(*a*)), which was attributed to the three-dimensional morphology of the carbides. The coarse microstructure of the cast alloy offered relatively large spaces between the carbides, where silica sand of small size could enter and plough. The sharp angularities of the sand particles could result in the material removal by microcutting. The fragments of the broken carbides due to the brittle fracture could also work as new abrasives, as indicated by the abrasive marks leading from the fragmented carbides (Fig. 6(*a*)). The pits on the matrix also illustrated denting by small sand particles or angularities, which could initiate fatigue cracks. All of these factors contributed to the material removal of the cast alloy. For the HIPed alloy, brittle fracture of the carbides was not appreciated from the observation of the worn surface (Fig. 6(*b*)), whereas ploughing was the main wear mechanism, as indicated by the abrasive marks in Fig. 6(*b*). The carbides were seen protruding from the matrix, indicating the preferential wear of the matrix, prior to the carbide pullout. The carbides in the HIPed alloy were too small to withstand ploughing due to their two-dimensional structures, as opposed to the three-dimensional eutectic net in the cast counterpart. The mechanism was similar to that previously reported [15], where carbide pullout and pit formation were the dominant wear mechanisms in fine carbide alloys.

The carbide morphology therefore significantly influenced the abrasive wear mechanisms, i.e., the brittle fracture on the carbides of the cast alloy and carbide pullout in the HIPed alloy. Two factors were responsible for the low tendency of carbides to fracture in the HIPed alloy: (1) the higher critical load for the onset of cracks, $w^*$, and (2) the lower normal load on a single carbide grain. As discussed earlier in Sec. 4.3, the impact energy of the HIPed alloy was almost an order of magnitude higher than that of the cast alloy, which generally indicated a much higher fracture toughness, $K_{1C}$, of the HIPed alloy, compared with its cast counterpart. Even if both alloys had a similar fracture or impact toughness, the cast alloy had a higher tendency to fracture due to the loading on its carbides. As both alloys had similar hardness, the critical load for the onset of cracks, $w^*$, (Eq. (5)) in the HIPed alloy, was higher than that of the cast alloy. Due to the finer microstructure of the HIPed alloy, the contact load applied by individual sand particles was shared between a number of carbides and the matrix. This can be understood from a simple calculation of the contact area ($2a$, Eq. (3)) formed at the interface of sand particles and alloy. As the sand particles were rounded, for an approximate calculation they can be modeled as spheres of 150 $\mu$m diameter ($2r$). Although it is almost impossible to know the exact number of sand particles, and the load shared by each of them within the contact region at a given time, a conservative approach can be adapted to assume that the loading ($w$) on a given sand particle, responsible for carbide cracking, can be of the order of 1% (1.3 N) of the total normal load (130 N) during the DSRW test. Based on this model, the contact diameter ($2a$) calculated from the Hertzian equation (Eq. (3)) of elastic loading can be approximated as $\geq 20$ $\mu$m. This area will grow further with the increase in sand particle diameter, increase in loading of individual particles, plasticity effects, frictional effects, and roll/slide ratio. Contact area of this dimension, based on a conservative model, therefore indicates that the contact diameter was an order of magnitude bigger than the carbide size (approximately $1-3$ $\mu$m) in the HIPed alloy. Hence individual carbide particles were only subjected to a small fraction of the total load on a given sand particle. Contrary to this, individual large blocky carbides in the cast alloy had to sustain a much higher contact load, as the entire contact area ($2a \geq 20$ $\mu$m) could be located on a single carbide particle ($5-20$ $\mu$m). Therefore there was a much higher probability that the loading resulting from such contact conditions on an individual carbide particle could exceed the critical value $w^*$ and result in the brittle fracture of the cast alloy.

The magnitude of contact stress approximated from Eq. (4) for this simplified model can be estimated to give a typical contact stress of approximately 5 GPa, which is high enough to fracture a carbide grain. However, despite significant fracture of carbides in the cast alloy, its abrasive wear performance was only slightly inferior to the HIPed alloy. This was because despite being fractured, some fragments of carbide remained interlocked within the matrix of the cast alloy due to the three-dimensional eutectic net. This prevented these fragments of cracked carbides from being pulled out, and hence did not contribute to the volume loss. However in the HIPed alloy, once the matrix was abraded by the abrasive sand particles, the carbides were easily pulled out due to their two-dimensional structure.

Results of this investigation also indicate that the wear volume loss marginally increased with decreasing particle size of the silica sand (Fig. 5). This was because the finer abrasive particles could enter and plough the matrix region more easily and result in more material removal. In this investigation, Sand A was slightly larger or similar in size to most of the coarse carbides in the cast alloy, whereas Sand B was generally larger than those carbides. Hence even smaller sand particles, than the ones considered in this investigation, can further elaborate the differences in the wear mechanisms of the cast and HIPed alloys.

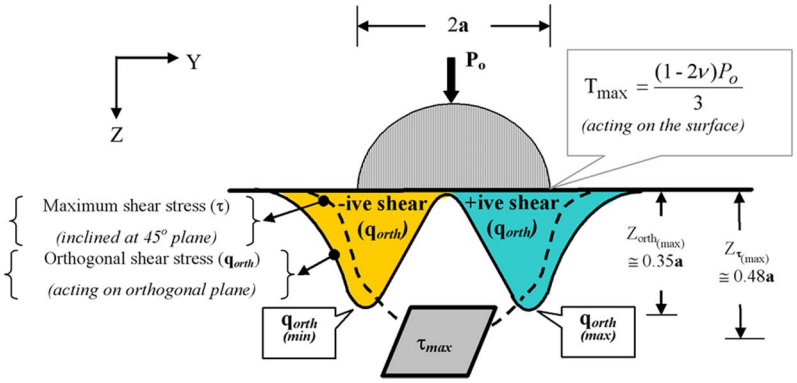


**Fig. 11 Schematic of the Hertzian stress distribution during the RCF test**

**4.5 Pin-On-Disk Wear Performance.** In the self-mated pin-on-disk tests on the cast alloys, the matrix on both the pin and the disk samples was worn preferentially. The remaining protruding carbides on the worn surface acted as asperities, and the contacts between them led to the removal of material. The wear mechanisms involved carbide ploughing on the matrix and brittle fracture of the carbides, as indicated by the abrasive grooves and the cracks on the carbides shown in Figs. 8(*a*) and 8(*b*). A number of grooves were observed on the wear scars of the HIPed pin and disk samples (Figs. 8(*c*) and 8(*d*)), indicating that ploughing was the main wear mechanism. The width and depth of some grooves was such that a number of carbides were ploughed away together with the matrix. Some small pits could also be observed on the worn surface due to carbide pulled out. The wear debris collected after the tests for both alloys were finer than the typical grooves observed in Figs. 8(*a*) and 8(*c*), indicating that they spent some time in the contact region.

Although the total volume loss of both alloys was similar, the cast disk suffered more volume loss than the HIPed disk, while the cast pin suffered less wear than the HIPed pin. This can be attributed to the three-dimensional structure of the coarse carbides in the cast alloy. The observation on the worn surface (Fig. 8(*a*)) showed that the debris were interlocked on the cast pin, as the abrasive grooves were terminated by the coarse carbides and did not run the entire length of the pin surface. Hence the debris embedded on the cast pin shared the load, which reduced the pin wear, while the debris in the contact region resulted in three-body abrasion behavior, which significantly increased the wear of disk material. Contrary to this, the grooves on the HIPed pin and disk (Figs. 8(*c*) and 8(*d*)) ran almost the entire length of the wear scar, where debris could roll/slide easily within these grooves. Carbide embedding in the pin material was therefore not significant in the HIPed alloy, hence there was no preference in the wear of either the disk or pin for the HIPed alloy.

**4.6 Ball-On-Flat Wear Performance.** In the sliding wear tests against the WC-Co ball, the cast alloy disk showed better wear resistance than the HIPed alloy, which was attributed to the coarse microstructure of the cast alloy. During the tests, the hard WC-Co ball could plough through the alloy sample. The matrix was worn preferentially, and cracks initiated and propagated on the carbides after cyclic loading. As discussed earlier, the carbides in the cast alloy were coarse and interlocked in the matrix. Even after a carbide fractured, it could still be retained in the matrix due to the three-dimensional eutectic net in the cast alloy, as indicated in Fig. 8(*e*). Therefore the carbides in the cast alloy resisted ploughing and reduced wear loss. However for the HIPed alloy, the fine carbides could not withstand ploughing, as indicated by the grooves on the worn surface (Fig. 8(*f*)). These grooves were so wide that a number of carbides could be ploughed away together with the matrix in a single groove and formed plate-like debris.

The WC-Co ball also had of a number of carbides in its microstructure. These carbides were much smaller (typically 2 $\mu$m, manufacturer's data) than the carbides in the cast alloy, resulting in the appreciable wear of the WC-Co ball. However, the carbides in the HIPed alloy were similar in size to those in the WC-Co ball, resulting in negligible wear of the WC-Co ball. The cast alloy had much bigger carbides than the WC-Co ball material, which resulted in the appreciable wear of the WC-Co ball when compared with the HIPed counterpart. Although this ball wear was nonuniform and could not be quantified, the higher volume loss of the ball wearing against the cast alloy should ultimately reduce the difference in the total wear loss of the test couples (Fig. 7) for both alloys. The trend of this relative wear performance and underpinning wear mechanisms was similar to that observed for Stellite 20 alloys [20].

**4.7 Contact Fatigue Performance.** RCF tests provide an evaluation of the impact and fatigue behavior of the material under high strain rates and under high stress (Hertzian) contact conditions. The relative velocity during loading and unloading was of the order of 6 m/s which was higher than the Charpy impact tests (4 m/s), whereas the stress distribution was Hertzian in the RCF tests. The contact fatigue tests used in the current investigation served two main purposes. First, the failure modes generally seen in these tests, e.g., micro- and/or macropitting, spalling, delamination, etc. [25,41], are similar to those observed in most of the tribological applications of engineering alloys, as these failures rely on the localized stress distribution to initiate and propagate fatigue cracks due to imperfections in the material's microstructure. Second, the high stress and high strain rate during these tests provide some insights about their impact behavior. Various theories were presented in published literature to understand these underpinning failure mechanisms [25,41–44]. The most common theories rely on the depth of either the maximum (Eq. (2)) or orthogonal (Eq. (1)) shear stress for subsurface failures, or on the maximum tensile stress at the edge of contact region for surface initiated failures, as represented in Fig. 11.

The SEM investigations of the wear tracks indicated that generally the cast alloy failed via delamination, whereas the failure mode for the HIPed counterpart was spalling (Fig. 10). This difference in failure mode is not consistent to what was observed for the Stellite 20 alloys [20], where spalling and surface distress were observed for the cast and HIPed alloys, respectively. Surface initiated failure, which generally occurred in the very near surface region of brittle materials, was not responsible for spalling or delamination of Stellite 6 alloys, as the depths of failure for these alloys were either near or deeper than the depth of maximum shear stress (Table 4). Hence cracks initiated in the subsurface region, either due to alloy imperfections or due to cyclic loading during fatigue testing, and grew in the subsurface to longer

lengths before changing their direction toward the surface. Similar to the crack propagation mechanisms discussed earlier in Secs. 4.3 and 4.4, the fatigue cracks in the HIPed alloy propagated through the metal matrix and at the carbide/matrix boundary, which resisted crack propagation, whereas in the cast alloy the fatigue cracks propagated along the three-dimensional eutectic net, which provided a relatively easy propagation route. Hence the finer microstructure of the HIPed alloy resulted in an improved contact fatigue performance than its cast counterpart. The widths of the wear tracks (typically 600 $\mu$m) were greater than the computed contact widths (Eq. (3), Table 4), which could be attributed to the plastic deformation, rolling wear, and the influence of material shakedown during the first few cycles of testing [45,46]. In comparison to the previously reported investigation of Stellite 20 alloys [20], it is worth noting that the relative performance of the HIPed Stellite 20 alloy was superior to that of Stellite 6 alloys. It is also worth appreciating that the maximum contact stress for the RCF test with Stellite 6 alloys varied between 1.9 GPa and 2.7 GPa, whereas this stress level was higher (3.1–3.6 GPa) for the Stellite 20 alloys, indicating that for similar stress levels Stellite 20 would perform considerably superior when compared with the Stellite 6 alloy. This reduction in fatigue performance is not consistent with the order of magnitude increase in toughness observed in the Stellite 6 alloy (Table 3). Hence, in comparing the RCF performance and failure modes of HIPed Stellite 6 and 20 alloys, a reduction in hardness and carbide fraction of 41% and 63%, respectively, had a more detrimental effect than the expected improvement on the basis of order of magnitude increase in the impact toughness. The rationale behind this difference in the expected trend is attributed to the higher hardness and carbide fraction of HIPed Stellite 20 alloy, which helps support the contact load, and also modifies the material's shakedown behavior [46]. This is consistent with previous investigations where a reduction in hardness (or softening) of the contact pair is shown to influence the RCF performance of the bearing steels [25]. Hence a complex interdependency of hardness, toughness, carbide fraction, and carbide morphology dictates the RCF performance and failure modes of these alloys, and indications on the basis of impact resistance performance alone may not translate directly to the improvement in fatigue performance. HIPed Stellite 20 is more suitable for even higher stress levels of loading ($>3$ GPa) than the HIPed Stellite 6 alloy ($\leq 2$ GPa). These stress levels are however much higher than those sustainable by the cast alloys. These results indicated that Stellite 6 alloys could substantially benefit from the HIPing process in terms of impact and fatigue performance, without sacrificing their hardness, abrasive, and sliding wear resistance. However, its fatigue performance was lower than that of the HIPed Stellite 20 alloy.

## 5 Conclusions

This investigation considered the structure-property relationships and tribomechanical evaluations of Stellite 6 alloys produced by two different manufacturing processes of HIPing and casting. The results of this investigation indicated that changing the manufacturing process to HIPing can make Stellite 6 alloys suitable for high stress applications. Similarly, variations in alloying elements also had considerable influence on the tribomechanical properties of these cobalt-based alloys. The specific conclusions can be summarized as follows.

(1) The impact toughness and the contact fatigue performance of the HIPed alloy were significantly higher than that of the cast alloy. The improvement in the impact toughness and fatigue resistance of the HIPed alloy was attributed to its relatively finer microstructure, which arrested crack propagation.
(2) In comparison to the HIPed Stellite 20 alloys, although there was an order of magnitude improvement in the impact toughness of the HIPed Stellite 6 alloy, the fatigue performance was lower than that of the HIPed Stellite 20 alloy. Hence a complex interdependency of hardness, toughness, carbide content, and morphology dictate RCF performance, and expected performance gains on the basis of impact resistance performance alone may not translate directly to an improvement in RCF performance.
(3) The cast and HIPed Stellite 6 alloys showed similar average hardness, which was 41% lower than that of Stellite 20 alloy. The abrasive and sliding wear resistance of both HIPed and cast Stellite 6 alloys were also similar. Brittle fracture of the carbides and ploughing of the matrix were the main wear mechanisms for the cast alloy, whereas for the HIPed alloy, ploughing and carbide pullout were the dominant wear mechanisms. This was consistent with what was previously observed for Stellite 20 alloys.
(4) The HIPed Stellite 6 alloy had a much finer microstructure than the cast alloy, which showed a hypoeutectic microstructure. The microstructural phases, i.e., $\alpha$-cobalt, $M_7C_3$, $Co_3W$, and $Co_7W_6$, were identified in both alloys, while $Co_6W_6C$ was identified only in the cast alloy.
(5) The main fatigue failure mode was delamination for the cast and spalling for the HIPed Stellite 6 alloy. This difference in the failure mode was attributed to the differences in the microstructure of the two alloys.

## References


[1] Crook, P., 1994, "Cobalt-Base Alloys Resist Wear, Corrosion, and Heat," Advanced Materials & Processes, **145**(4), pp. 27–30.
[2] Antony, K. C., 1983, "Wear-Resistant Cobalt-Based Alloys," J. Met., **5**(2), pp. 52–60.
[3] Frenk, A., and Kurz, W., 1994, "Microstructural Effects on the Sliding Wear Resistance of a Cobalt-Based Alloy," Wear, **174**, pp. 81–91.
[4] Berns, H., and Wendl, F., 1985, "Microstructure and Properties of CoCr29W (Stellite 6) in the As-Cast, Forged and Powder Metallurgical Condition," *Proceedings of the Second International Conference on Cobalt*, Venice, Italy, pp. 292–305.
[5] Crook, P., 1991, "Cobalt and Cobalt Alloys," *ASM Handbook*, ASM Materials Park, OH, Vol. 2, pp. 446–454.
[6] Shin, J. C., Doh, J. M., Yoon, J. K., Lee, D. Y., and Kim, J. S., 2003, "Effect of Molybdenum on the Microstructure and Wear Resistance of Cobalt-Base Stellite Hardfacing Alloys," Surf. Coat. Technol., **166**, pp. 117–126.
[7] Kuzucu, V., Ceylan, M., Celik, H., and Aksoy, I., 1998, "An Investigation of Stellite-6 Alloy Containing 5.0 Wt% Silicon," J. Mater. Process. Technol., **79**, pp. 47–51.
[8] Wang, L. C., and Li, D. Y., 2003, "Effects of Yttrium on Microstructure, Mechanical Properties and High-Temperature Wear Behavior of Cast Stellite 6 Alloy," Wear, **255**, pp. 535–544.
[9] De Mol van Otterloo, J. L., and De Hosson, J. T. M., 1997, "Microstructure and Abrasive Wear of Cobalt-Based Laser Coatings," Scr. Mater., **36**, pp. 239–245.
[10] Crook, P., and Levy, A. V., 1992, "Friction and Wear of Cobalt-Base Wrought Alloys," *ASM Handbook*, ASM, Materials Park, OH, Vol. 18, pp. 766–771.
[11] Klarstrom, D. L., 1993, "Wrought Cobalt-Base Superalloys," J. Mater. Eng. Perform., **2**(4), pp. 523–530.
[12] Kim, H. J., and Kim, Y. J., 1999, "Wear and Corrosion Resistance of PTA Weld Surfaced Ni and Co Based Alloy Layers," Surf. Eng., **15**(6), pp. 495–501.
[13] Silence, W. L., 1978, "Effect of Structure on Wear Resistance of Co-, Fe-, and Ni-Base Alloys," ASME J. Lubr. Technol., **100**, pp. 428–435.
[14] Kosel, T. H., Li, S. Z., and Rao, C. M., 1985, "The Size Effect in Abrasion of Dual-Phase Alloys," ASLE Trans., **28**(3), pp. 343–350.
[15] Desai, V. M., Rao, C. M., Kosel, T. H., and Fiore, N. F., 1984, "Effect of Carbide Size on the Abrasion of Cobalt-Base Powder Metallurgy Alloys," Wear, **94**, pp. 89–101.
[16] Yang, L. J., and Loh, N. L., 1995, "The Wear Properties of Plasma Transferred Arc Cladded Stellite Specimens," Surf. Coat. Technol., **71**, pp. 196–200.
[17] Cooper, D., Davis, F. A., and Wood, R. J. K., 1992, "Selection of Wear-Resistant Alloys for the Petrochemical Industry," J. Phys. D, **25**, pp. A195–A204.
[18] Song, J. H., and Kim, H. J., 1997, "Sliding Wear Performance of Cobalt-Based Alloys in Molten-Al-added Zinc Bath," Wear, **210**, pp. 291–298.
[19] De Mol van Otterloo, J. L., and De Hosson, J. T. M., 1997, "Microstructural Features and Mechanical Properties of a Cobalt-Based Laser Coating," Acta Mater., **45**, pp. 1225–1236.
[20] Yu, H., Ahmed, R., and De Villiers Lovelock, H., 2007, "A Comparison of the Tribo-Mechanical Properties of Wear-Resistant Cobalt Based Alloys Produced by Different Manufacturing Processes," ASME J. Tribol., **129**, pp. 586–594.
[21] Kumar, P., 1986, "Properties of P/M Stellite Alloy No. 6," Progress in Powder Metallurgy, **41**, pp. 415–437.

[22] ASTM G65-00, 2000, "Standard Test Method for Measuring Abrasion Using the Dry Sand/Rubber Wheel Apparatus," ASTM International, West Conshohocken, PA.
[23] ASTM G133-02, 2002, "Standard Test Method for Linearly Reciprocating Ball-on-Flat Sliding Wear," ASTM International, West Conshohocken, PA.
[24] Stewart, S., Ahmed, R., and Itsukaichi, T., 2004, "Contact Fatigue Failure Evaluation of Post-Treated WC-NiCrBSi Functionally Graded Thermal Sprayed Coatings," Wear, **257**, pp. 962–983.
[25] Shipley, R. J., and Becker, W. T., 2002, "Failure Analysis and Prevention," *ASM Handbook*, ASM, Materials Park, OH, Vol. 11, Sec. 6E.
[26] Hutchings, I. M., 1992, *Tribology: Friction and Wear of Engineering Alloys*, Edward Arnold, London, UK.
[27] Ashworth, M. A., Bryar, J. C., Jacobs, M. H., and Davies, S., 1999, "Microstructure and Property Relationships in Hipped Stellite Powders," Powder Metall., **42**(3), pp. 243–249.
[28] Ayagaki, M., Ohishi, T., Izumi, S., and Tanaka, T., 1996, "Development of Superior Resistant Alloys by HIP Process and Their Applications," Nippon Steel, Technical Report No. 68.
[29] Dawson, R. J., and Foley, E. M., 1990, "P/M Cobalt-Base Wear-Resistant Alloys," *ASM Handbook*, ASM, Materials Park, OH, Vol. 1, pp. 977–980.
[30] De Brouwer, J. L., and Coutsouradis, D., 1966, "Influence of Tungsten and Carbon Contents on the Microstructure and Properties of a Cobalt-Base Hardfacing Alloy," Cobalt (Engl. Ed.), **32**, pp. 141–147.
[31] Ghar, K. Z., 1987, *Microstructure and Wear of Alloys*, Elsevier, New York, pp. 36–38.
[32] Schindler, H. J., 2000, "Relation Between Fracture Toughness and Charpy Fracture Energy: An Analytical Approach," *Proceedings of the 1999 Symposium on Pendulum Impact Testing: A Century of Progress*, ASTM, pp. 337–353.
[33] Schindler, H. J., and Morf, U., 1993, "Closer Look at Estimation of Fracture Toughness From Charpy V-Notch Tests," Int. J. Pressure Vessels Piping, **55**(2), pp. 203–212.
[34] British Standard, 1991, *PD 6493: Guidance on Methods for Assessing the Acceptability of Flaws in Fusion Welded Structures*, BSI, London, UK.
[35] Underwood, J. H., and Leger, G. S., 1984, "Fracture Toughness of High Strength Steel Predicted From Charpy Energy or Reduction in Area," *Proceedings of the Fracture Mechanics: Fifteenth Symposium*, ASTM STP833, Maryland, R. J. Sanford, ed., ASTM Paper No. STP32570S, pp. 481–498.
[36] Habashi, M., Miannay, D., Tvrdy, M., and Galland, J., 1984, "Correlation Between Apparent Toughness K//A and Charpy Impact Energy in High and Low Strength Steels," *Advances in Fracture Research*, *Proceedings of the Sixth International Conference on Fracture (ICF6)*, New Delhi, India, pp. 1551–1558.
[37] Holzmann, M., Dlouhy, I., Vlach, B., and Krumpos, J., 1996, "Degradation of Mechanical Properties of Cr–Mo–V and Cr–Mo–V–W Steam Turbine Rotors After Long Term Operation at Elevated Temperatures: Part II. Fracture Toughness, Correlation of Fracture Toughness With Charpy V-Notch Results," Int. J. Pressure Vessels Piping, **68**, pp. 113–120.
[38] Schmitt, W., Sun, D. Z., Bohme, W., and Nagel, G., 1994, "Evaluation of Fracture Toughness Based on Results of Instrumented Charpy Tests," Int. J. Pressure Vessels Piping, **59**(1–3), pp. 21–29.
[39] Sreenivasan, P. R., Moitra, A., Ray, S. K., Mannan, S. L., and Chandramohan, R., 1996, "Dynamic Fracture Toughness Properties of a 9Cr–1Mo Weld From Instrumented Impact and Drop-Weight Test," Int. J. Pressure Vessels Piping, **69**, pp. 149–159.
[40] Lee, O. S., Hong, S. K., Park, W. K., and Hwang, S. K., 1995, "Dynamic Crack Initiation Toughness by Instrumented Charpy Impact Tests in Highly Brittle Alloys," *Proceedings of the ASME Pressure Vessel Piping Divison*, Vol. 300, pp. 63–68.
[41] Tallian, T. E., 1967, "On Competing Failure Modes in Rolling Contact," ASLE Trans., **10**, pp. 418–439.
[42] Hadfield, M., Stolarski, T. A., and Cundill, R. T., 1993, "Failure Modes of Ceramics in Rolling Contact," Proc. R. Soc. London, Ser. A, **443**, pp. 607–621.
[43] Ahmed, R., and Hadfield, M., 2002, "Mechanisms of Fatigue Failure in Thermal Spray Coatings," J. Therm. Spray Technol., **11**(3), pp. 333–349.
[44] Tallian, T. E., and McCool, J. I., 1971, "An Engineering Model of Spalling Fatigue in Rolling Contact—The Surface Model and Engineering: Discussion and Illustrative Examples," Wear, **17**, pp. 447–480.
[45] Kapoor, A., and Williams, J. A., 1996, "Shakedown Limits in Rolling-Sliding Point Contacts on an Anisotropic Half-Space," Wear, **191**, pp. 256–260.
[46] Wong, S. K., Kapoor, A., and Williams, J. A., 1997, "Shakedown Limits on Coated Surfaces," Thin Solid Films, **292**, pp. 156–163.